Applied Catalysis B: Environmental 237 (2018) 633–640

Contents lists available at ScienceDirect

Applied Catalysis B: Environmental

journal homepage: www.elsevier.com/locate/apcatb

# Ultrathin nanosheets g-$C_3N_4$@$Bi_2WO_6$ core-shell structure *via* low temperature reassembled strategy to promote photocatalytic activity

Yingying Wang, Wenjun Jiang, Wenjiao Luo, Xianjie Chen, Yongfa Zhu*

*Department of Chemistry, Tsinghua University, Beijing 100084, PR China*

ARTICLE INFO

*Keywords:*
Photocatalysis
Ultrathin g-$C_3N_4$
$Bi_2WO_6$ nanosheet
Core-shell structure
Interface catalytic system

ABSTRACT

In this work, ultrathin nanosheet g-$C_3N_4$@$Bi_2WO_6$ core-shell structure is fabricated by a new method of CN precursor *in situ* coating and low temperature reassembled. The CN small molecules were successfully polymerized to form ultrathin g-$C_3N_4$ layer (about 1 nm) on the surface of $Bi_2WO_6$ nanosheet under low temperature. And the g-$C_3N_4$@$Bi_2WO_6$ photocatalyst with 1 nm thickness of shell layers has the highest photocatalytic degradation phenol activity with visible light irradiation which is almost 5.7 times as high as that of bulk g-$C_3N_4$ and also 1.9 times compare to $Bi_2WO_6$ nanosheet. Simultaneously, phenol degradation activity by using g-$C_3N_4$@$Bi_2WO_6$ photocatalyst under full spectrum is 3.3 times that of bulk g-$C_3N_4$ and 1.5 times that of $Bi_2WO_6$ nanosheet. Superoxide radicals ($\cdot O_2^-$) and hydroxyl radicals ($\cdot OH$) as the main oxidative species proved by electron spin resonance spectroscopy (ESR). The interface catalytic system was found, that is the interface between the $Bi_2WO_6$ core and g-$C_3N_4$ shell effectively promote the phenol degradation activity revealed through a comprehensive contrast experiment. The establishment of g-$C_3N_4$@$Bi_2WO_6$ core-shell catalytic system can offer blueprints for the construction of other new interface catalytic system.

## 1. Introduction

$Bi_2WO_6$ as an excellent visible light driven photocatalyst with a narrow band gap (~2.8 eV) [1] and suitable energy band positions possess many advantages such as high activity, thermal and chemical stability, which ascribes to the unique layered structures that accumulated layers of alternating the $WO_6$ octahedron nanosheets and $(Bi_2O_2)^{2+}$ layers [2–4]. Because of its unique alternating layered structures, $Bi_2WO_6$ has the large internal electric field and asymmetrical polarization effect which leads to an essential reason for exhibiting the excellent visible light catalytic activity. Similar to other two-dimensional nanomaterials, $Bi_2WO_6$ not only exhibits higher surface area and more photocatalytic active sites [5] but also exhibits fascinating face-dependent catalytic properties [6], which could also significantly decrease the distance of the photogenerated charge transfer and facilitate better carriers migration from the interior to the surface [7,8]. $Bi_2WO_6$ has attracted more attention on the photocatalytic degradation of organic pollutants [9–12] and energy conversion [13,14] due to its unique crystal structure, reactivity and stability.

However, pure $Bi_2WO_6$ nanosheet has a photo-absorption region from UV to the visible light shorter than 450 nm, which accounts for a small part of the solar spectrum [15]. What's more, fast recombination rate of electron-hole pairs significantly restricts its energy conversion efficiency. Therefore, a large number of studies have focused on the noble metal doping [16], non-noble metal doping [17,18] and building hybrid structure [19,20] to change the electronic structure and intrinsic properties of $Bi_2WO_6$ materials. Among all the methods, building the specific interface between two well matched photocatalysts with different energy levels is a promising strategy, which can realize the effective charge transfer at the interface to promote the separation of photogenerated electrons-holes resulting an enhancement photocatalytic activity. In 2009, g-$C_3N_4$ was firstly reported by Wang et al. [21] as a metal-free photocatalyst for producing hydrogen from splitting water with visible light irradiation. Then g-$C_3N_4$ gains increasing attention as an attractive material in the field of photocatalysis by researchers, because of its good visible light activity, thermal stability and chemical stability [22–28]. In our previous work [29–32], it was revealed that the formation of organic-inorganic core-shell structure can extraordinarily accelerate the separation of photogenerated carriers resulting significant enhancement of the photocatalytic activity. Especially in our recent study [33], the g-$C_3N_4$@$TiO_2$ core-shell structure photocatalyst with controlled ultrathin g-$C_3N_4$ layer was prepared by the sol-gel approaches *in situ* coating re-assembled, successfully controlling internal electric field in the interface of the core-shell structure which dramatically promotes the photocatalytic activity. However, there still exist some shortcomings in the method. The g-$C_3N_4$ bulk

* Corresponding author.
*E-mail address:* zhuyf@mail.tsinghua.edu.cn (Y. Zhu).

https://doi.org/10.1016/j.apcatb.2018.06.013
Received 9 March 2018; Received in revised form 1 June 2018; Accepted 4 June 2018
Available online 04 June 2018

phase material must be protonated by the process of strong oxidizing acid $HNO_3$ and then it needs high-temperature heating process during re-polymerization which are demonstrated to be not friendly to environment and exist potential safety problems. Therefore, it is very significant to develop a new method of using neutral condition and low temperature process to prepare the core-shell structure.

In this work, the g-$C_3N_4$ bulk phase material was cut into CN transparent precursor by the process of neutral hydrothermal reaction using water as solvent and then *in situ* coating low temperature catalytic polymerization to fabricate ultrathin nanosheet g-$C_3N_4$@$Bi_2WO_6$ core-shell structure with controlled g-$C_3N_4$ shell. CN small molecules were successfully reassembled on the surface of $Bi_2WO_6$ nanosheet to form ultrathin g-$C_3N_4$ layer (about 1 nm) under low temperature proved by Solid-state nuclear magnetic resonance (13C-NMR) and Fourier transform infrared spectra (FT-IR). The results show that the g-$C_3N_4$@$Bi_2WO_6$ core-shell sample with 1 nm shell thickness has the highest visible light photocatalytic activity which is almost 5.7 times as high as that of bulk g-$C_3N_4$ and 1.9 times that of $Bi_2WO_6$ nanosheet. Simultaneously, phenol degradation activity of g-$C_3N_4$@$Bi_2WO_6$ photocatalyst under full spectrum is 3.3 times that of bulk g-$C_3N_4$ and 1.5 times that of $Bi_2WO_6$ nanosheet. A large area uniform g-$C_3N_4$@$Bi_2WO_6$ core-shell structure were clearly observed by TEM and the core-shell structure in the catalytic process effectively promote the phenol degradation activity revealed through a comprehensive contrast experiment. The mechanism of the enhancement activity of g-$C_3N_4$@$Bi_2WO_6$ core-shell photocatalyst and the main oxidative active species in the catalytic process were elucidated by photoluminescence spectroscopy (PL) and electron spin resonance spectroscopy (ESR) characterization techniques. The repetitive experiment and cycle experiment show that the g-$C_3N_4$@$Bi_2WO_6$ photocatalyst prepared by the new method has a well repeatability and stability which is convenient for recovery.

## 2. Experimental

### 2.1. Preparation of g-$C_3N_4$@$Bi_2WO_6$ core-shell structure photocatalyst

Dicyandiamide was purchased from Beijing Chemical Reagent Corp., PR China. All other reagents used in this research were analytical pure and used without further purification.

The $Bi_2WO_6$ nanosheet was prepared by a typical hydrothermal reaction using water as solvent. The detailed preparation steps were as follows: 0.005 mol $Bi(NO_3)_3{\cdot}5H_2O$ and 0.0025 mol $Na_2WO_4$ were dissolved in 30 mL deionized water. The resulting white solution was transferred into a Teflon-lined stainless-steel autoclave and heated at 180 °C for 24 h. The $Bi_2WO_6$ nanosheet were collected and washed several times with deionized water before being dried at 60 °C for 12 h.

The g-$C_3N_4$ was prepared by a typical pyrolysis of dicyandiamide in air atmosphere. The detailed preparation steps were as follows: 10 g dicyandiamide were put in a Muffle Furnace and heated to 550 °C at a heating rate of 2.3 °C/min and calcined at 550 °C for 4 h. The yield of the optimum g-$C_3N_4$ was about 40%.

Preparation of CN transparent precursor: 0.5 g g-$C_3N_4$ powder were dispersed in 20 mL deionized water then placed into a Teflon-lined stainless-steel autoclave and heated at 210 °C for 6 h.

Preparation of g-$C_3N_4$@$Bi_2WO_6$ core-shell photocatalyst: A certain amount of $Bi_2WO_6$ nanosheet powder was added to the CN transparent precursor. The solvent was slowly removed by freeze-drying process. 13 wt% g-$C_3N_4$@$Bi_2WO_6$ core-shell photocatalyst (100, 150, 200, 250, 300 °C) were obtained by annealing of the samples at different temperatures in a tube furnace under $N_2$ protection for 4 h. The CN@$Bi_2WO_6$ samples (13 wt%, 23 wt%, 37 wt%) were calcined at 200 °C for 4 h to obtain g-$C_3N_4$@$Bi_2WO_6$ core-shell structure photocatalyst with different mass fractions.

### 2.2. Characterizations

The morphologies of the g-$C_3N_4$@$Bi_2WO_6$ core-shell photocatalyst were obtained by JEM 2010 transmission electron microscopy (TEM) operated at an accelerating voltage of 100 Kv and JEM-2011F field emission transmission electron microscopy with an accelerating voltage of 200 kV. The crystallinity of the g-$C_3N_4$@$Bi_2WO_6$ core-shell photocatalyst were characterized by X-ray diffraction (XRD) on Rigaku D/max-2400 X-ray diffractometer with Cu Kα radiation (λ = 1.5406 Å), the scanning range was 5–70°. 13C NMR was carried out on JNM-ECZ600R solid-state NMR with the probe diameter 3.2 mm, 12 kHz rotating speed and 2 s relaxation time. The UV–vis diffuse reflectance spectroscopy were recorded on Hitachi UV-3010 UV–vis spectrophotometer, using $BaSO_4$ as the reference sample. FT-IR were performed on Bruker VERTEX-70 spectrometer in the range of 4000 $cm^{-1}$ to 600 $cm^{-1}$ with a resolution of 1 $cm^{-1}$. Raman spectra were carried out using a HORIBA HR 800 microscopic confocal Raman spectrometer with an excitation of 514.5 nm laser light. PL were characterized by LS55 fluorescence spectrometer (Perkin-Elmer, USA) with a maximum excitation wavelength of 370 nm and a scanning wavelength range of 400–600 nm. The photocurrents were measured on an CHI 660B electrochemical system. The active species of phenol degradation can be detected by ESR (JEOL JES-FA200 EER) using 5, 5-dimethyl-1-pyrroline N-oxide (DMPO) as free radical trapping agent.

### 2.3. Photocatalytic experiments

The catalytic activity of g-$C_3N_4$@$Bi_2WO_6$ core-shell photocatalyst was evaluated by the phenol degradation tested in multitube photocatalytic reactor XPA-7. Visible light source was obtained by a 500 W Xe lamp with a 420 nm cutoff filter, and the optical power density was controlled at an average of 23 mW/$cm^2$. A detailed process was as follows: 25 mg photocatalyst was added into 5 mg/L phenol solution, which was stirred under visible light irradiation. 3 mL of the reaction solution was taken every 60 min and the photocatalytic material was removed by centrifuge separation. The concentration of phenol contaminants was analysed by Shimadzu LC-20A high performance liquid chromatography (HPLC) with a Venusil XBP-$C_{18}$ and a UV detector operated at 270 nm. The mobile phase consisted of methanol and water (volume ratio: 55/45) at a flow rate of 1 mL/min.

## 3. Results and discussion

### 3.1. Fabrication of g-$C_3N_4$@$Bi_2WO_6$ core-shell structure

The g-$C_3N_4$@$Bi_2WO_6$ core-shell structure photocatalyst with ultrathin g-$C_3N_4$ layer were fabricated by a transparent CN precursor *in situ* coating and low temperature reassembled strategy illustrated in Scheme 1. Firstly, the bulk g-$C_3N_4$ was prepared by a typical pyrolysis of dicyandiamide in air atmosphere. Then, the bulk phase material was cut into CN small molecules transparent solution by the process of hydrothermal reaction with water as solvent, which is demonstrated as a green and highly efficient pathway for the sol processing of a stable g-$C_3N_4$ colloidal suspension. To generated the required number of g-$C_3N_4$ layer on the outer surfaces of $Bi_2WO_6$ nanosheet, a certain amount of $Bi_2WO_6$ nanosheet powder was added to the CN transparent solution to construct uniformly CN@$Bi_2WO_6$ core-shell structure. The CN@$Bi_2WO_6$ sample was re-polymerized in a tube furnace at 200 °C under $N_2$ protection. All of the g-$C_3N_4$@$Bi_2WO_6$ sample are uniformly core-shell structure, seen in Fig. 1.

The size and morphology of the prepared g-$C_3N_4$@$Bi_2WO_6$ core-shell structure photocatalyst were observed by TEM and HRTEM. $Bi_2WO_6$ nanosheets are monodisperse and uniform ultrathin nanosheets with average size of approximately 50 nm and thickness of about 5 nm, as shown in Fig. 1a. It can be seen in Fig. 1b that the CN transparent solution is coated on the surface of $Bi_2WO_6$ nanosheets to form a

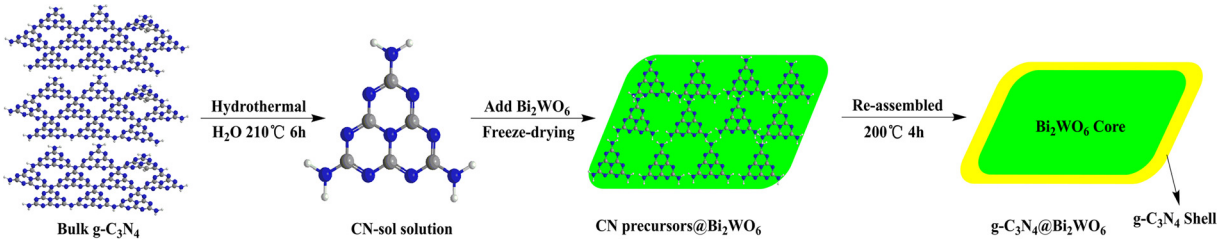


**Scheme 1.** Schematic illustration of preparation of g-$C_3N_4$@$Bi_2WO_6$ core-shell photocatalyst.

homogeneous CN@$Bi_2WO_6$ core-shell structure precursor. There exist two types CN@$Bi_2WO_6$ nanosheets which are the flat sample and the erected sample. In particular, core-shell structure in the erected sample is observed more clearly. As shown in Fig. 1c–e, a distinct g-$C_3N_4$@$Bi_2WO_6$ core-shell structure photocatalyst was successfully synthesized when CN@$Bi_2WO_6$ precursor was annealed at low temperature 100 °C, 150 °C and 200 °C. As can be seen in Fig. 1f–i, the measured lattice spacing on the crystal is 0.315 nm, which corresponds to the $Bi_2WO_6$ nanosheet (113) plane. The crystallinity of $Bi_2WO_6$ nanosheet is excellent, and the amorphous g-$C_3N_4$ layer (about 1 nm) of core-shell structure sample is significantly different from $Bi_2WO_6$ core.

In order to profoundly reveal whether the CN small molecules transparent solution could be re-polymerized into graphite phase conjugate structure at low temperature, a series of surface characterization techniques are carried out including XRD, FT-IR and solid-state NMR. Firstly, the CN precursor is annealed at the same experimental conditions and then tested for XRD. As can be seen from, Characteristic diffraction peaks for $Bi_2WO_6$ nanosheet (JCPDS, #73-1126) (Fig. 2a) are assigned to the (113), (200), (026), (313), (226) and (400) planes. The strong peak at around 27.4° is assigned to (002) plane of g-$C_3N_4$ crystal which corresponds to the inter-planar stacking of the CN aromatic system and the broad one at 13.0° is assigned to (100) plane which is attributed to triazine repeat units. It is noteworthy that there is almost no low-angle impurity peak in the XRD of g-$C_3N_4$@$Bi_2WO_6$ core-shell structure photocatalyst with calcination temperature between 100 °C and 300 °C, indicating that CN small molecules could be re-assembled on the surface of $Bi_2WO_6$ nanosheet. The peak intensities in the low-angle region gradually decrease with annealing temperature increasing from 100 °C to 250 °C, typically the peak intensities of 26.2° and 27.8° gradually decline and shift to high angle region (Fig. 2b). When the calcination temperature is raised to 300 °C, two typical characteristic peaks at 10.8° and 28.0° are obtained which are similar to the XRD characteristic peak of pure g-$C_3N_4$. This is further illustrated by subsequent FT-IR, NMR and Raman spectroscopy.

The solid-state 13C NMR spectrum of bulk g-$C_3N_4$ shows two typical peaks ranging from 155 to 175 [34–36], seen in Fig. 2e. However, the 13C NMR spectrum of the CN-200 °C sample shows a wide distribution of carbon peaks from 160 to 180 with a large chemical shift and no sharp main peak compared to bulk g-$C_3N_4$, indicating that there are many different kinds of chemical environments in the sample. It is concluded that the CN small molecules can't be re-polymerized into g-$C_3N_4$ alone under low calcination temperature. However, the 13C NMR

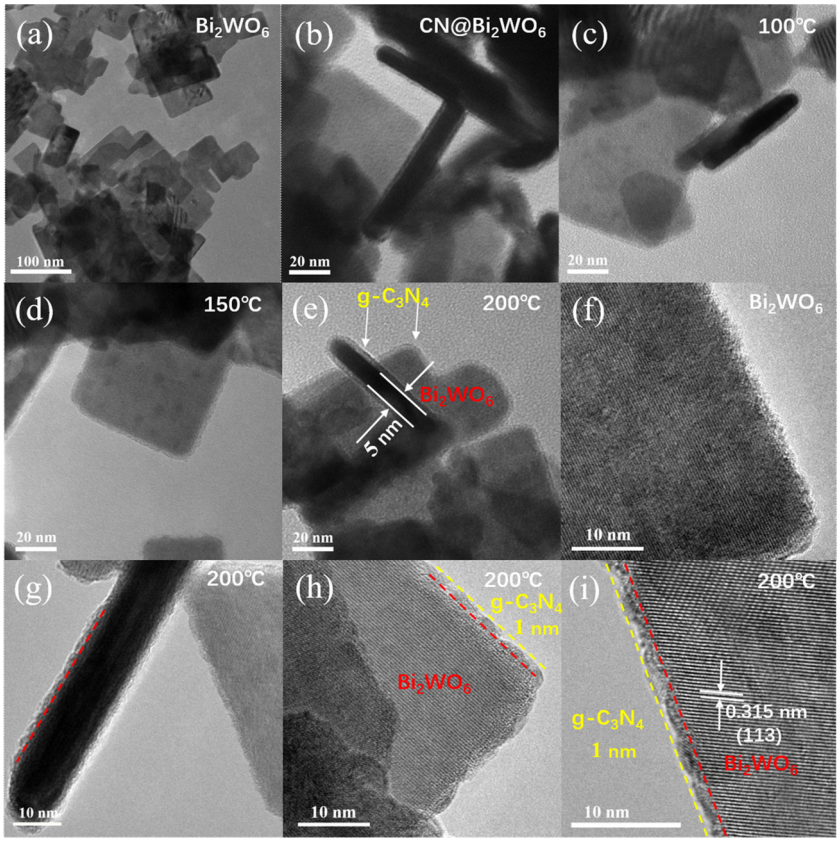


**Fig. 1.** (a–e) TEM image of $Bi_2WO_6$ and g-$C_3N_4$@$Bi_2WO_6$ core-shell photocatalyst; (f–i) HRTEM image of $Bi_2WO_6$ and g-$C_3N_4$@$Bi_2WO_6$ core-shell photocatalyst obtained at 200 °C.

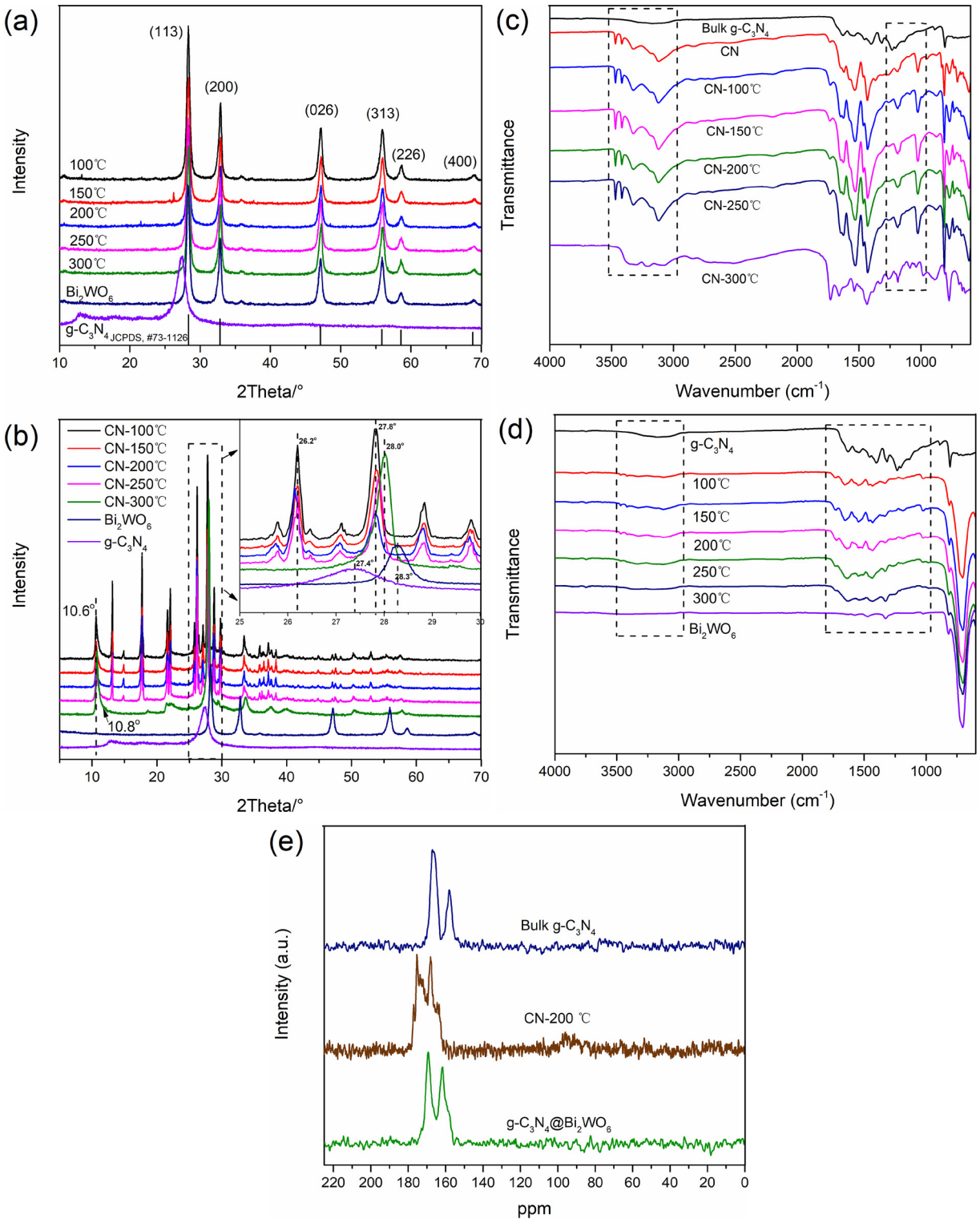


**Fig. 2.** g-$C_3N_4$@$Bi_2WO_6$ core-shell photocatalyst and CN precursor obtained at the same condition (a, b) XRD patterns and (c, d) FT-IR spectra; (e) 13C NMR spectra of Bulk g-$C_3N_4$, CN-200 ℃ and g-$C_3N_4$@$Bi_2WO_6$ core-shell photocatalyst obtained at 200 ℃.

spectrum of g-$C_3N_4$@$Bi_2WO_6$ core-shell photocatalyst are consistent with that of bulk g-$C_3N_4$, indicating that the CN small molecule can be re-polymerized into g-$C_3N_4$ at low temperature only when it is coated on the surface of $Bi_2WO_6$ nanosheet.

In order to further prove that CN precursors can be polymerized at low temperature only when it is coated on the surface of $Bi_2WO_6$ nanosheet system, the CN precursor is annealed at the same experimental conditions and then tested by FT-IR characterization technique. As shown in Fig. 2c, the broad peak around 3250 $cm^{-1}$ correlates with the degree of polymerization of pure g-$C_3N_4$. The strong peak region between 3000 $cm^{-1}$ and 3500 $cm^{-1}$ corresponds to the characteristic peaks of C–H and N—H. Several peaks in the range of 1200–1700 $cm^{-1}$ assigned to the typical stretching vibration of CN heterocycles, whereas the strong peaks in pure CN precursors are characteristic peaks of the melamine which are completely different from that of bulk g-$C_3N_4$. The result reveals that it is difficult to re-polymerize into large conjugated g-

$C_3N_4$ for pure CN precursors alone in the low temperature range below 300 °C. The g-$C_3N_4$@$Bi_2WO_6$ ultrathin nanosheet core-shell photocatalyst shows both the characteristic absorption peaks of g-$C_3N_4$ and $Bi_2WO_6$ nanosheet (Fig. 2d). And the significant red shift of the characteristic absorption peak of g-$C_3N_4$ is due to the fact that the original long-range orderly arrangement of pure g-$C_3N_4$ with a slight decline in the conjugation effect because of core-shell structure formed between g-$C_3N_4$ and $Bi_2WO_6$ nanosheet. This result adequately confirms the truth of low temperature catalytic polymerization into a large conjugated structure only in g-$C_3N_4$@$Bi_2WO_6$ catalytic system.

It can be seen from Fig. S1, the peaks of 305 $cm^{-1}$, 414 $cm^{-1}$, 712 $cm^{-1}$, 793 $cm^{-1}$ and 822 $cm^{-1}$ in the Raman spectrum are characteristic Raman shift of $Bi_2WO_6$ nanosheet [2]. Since g-$C_3N_4$ has strongly fluorescent under irradiation of the 514.5 nm excitation source, the characteristic Raman shift of $Bi_2WO_6$ nanosheet in g-$C_3N_4$@$Bi_2WO_6$ ultrathin nanosheet composite samples decreases with the polymerization degree of g-$C_3N_4$ increasing. The Raman spectra of composite samples at 100 °C and 150 °C exist the five characteristic Raman peaks of $Bi_2WO_6$ and showing a large blue shift which indicates that the formation of new chemical bonds at the interface of the core-shell structure and the role of separation and transfer of photogenerated charge in the photocatalytic process. Meanwhile, as can be seen in Fig. S2 the band edge of g-$C_3N_4$@$Bi_2WO_6$ ultrathin nanosheet core-shell structure photocatalyst in the UV–vis diffuse reflectance spectrum has red shift with the calcination temperature increasing. The spectral response of the core-shell structure photocatalyst annealing at 200 °C is the best. The result is consistent with the photocurrent of core-shell structure photocatalyst and the activity of phenol degradation under visible light.

As shown in Fig. S3, $Bi_2WO_6$ nanosheet shows a weight loss region between 230 °C and 270 °C which is very little weight loss during this temperature range due largely to desorption and decomposition of surface bound water. The weight loss region of pure g-$C_3N_4$ from 550 °C to 730 °C between assigned to the decomposition combustion of g-$C_3N_4$. Three regions of weight loss are observed both in CN@$Bi_2WO_6$ precursors and g-$C_3N_4$@$Bi_2WO_6$ core-shell photocatalysts. The first region of weight loss appeares at 280 °C, due to the decomposition of a small amount of ammonium salt formed in the CN transparent solution. The second weight loss region at 350 °C is attributed to the thermal decomposition of CN small molecules and the third weight loss region at 420 °C is attributed to the thermal decomposition of a small number of highly polymerized CN fragments. From the differential thermal analysis, it can be seen that the endothermic peak between 550 °C and 730 °C of the pure g-$C_3N_4$ sample corresponds to the decomposition combustion of g-$C_3N_4$. In g-$C_3N_4$@$Bi_2WO_6$ core-shell photocatalysts, the endothermic peaks at 280 °C, 350 °C and 420 °C, respectively correspond to the first, second and third regions of weight loss on the TGA curves. This result well explains that the activity of g-$C_3N_4$@$Bi_2WO_6$ core-shell photocatalyst dramatically decrease when the annealing temperature continues to increase above 200 °C.

### 3.2. Photocatalytic activity and photocurrent response

The phenol degradation and photocurrent response test under visible light and full spectrum were evaluated to reveal the photocatalytic activity of g-$C_3N_4$@$Bi_2WO_6$ core-shell catalyst. As shown in Fig. 3a, g-$C_3N_4$@$Bi_2WO_6$ core-shell photocatalyst under visible light irradiation exhibits excellent activity than that of bulk g-$C_3N_4$ and $Bi_2WO_6$ nanosheet. The photocatalytic activity of g-$C_3N_4$@$Bi_2WO_6$ core-shell photocatalyst is gradually enhanced with the annealing temperature increasing, which shows an order of 200 > 150 > 100 > 250 > 300 °C. Especially the degradation activity of g-$C_3N_4$@$Bi_2WO_6$ annealed at 200 °C exhibits 5.7 times higher than that of bulk g-$C_3N_4$ and 1.9 times higher than that of $Bi_2WO_6$ nanosheet. The result shows that CN precursor has the optimal degree of re-assembled on the surface of $Bi_2WO_6$ nanosheet when the annealing temperature is 200 °C. According to the data of the subsequent TGA, when the temperature is higher than 250 °C CN small molecules begin to be thermally decomposed resulting a dramatically decrease in activity. As shown in Fig. 3b, under full spectrum conditions the degradation activity of the g-$C_3N_4$@$Bi_2WO_6$ core-shell structure is in well accordance with that of visible light irradiation. The g-$C_3N_4$@$Bi_2WO_6$ core-shell structure catalyst obtained at 200 °C has the best activity which is 1.5 times than that of $Bi_2WO_6$ nanosheet and 3.3 times than that of bulk g-$C_3N_4$. As can be seen from the comparative experiment of Fig. S5, g-$C_3N_4$/$Bi_2WO_6$ is a contrast sample obtained by physically mixing and $Bi_2WO_6$-2 is prepared by the same solution treatment and calcination at 200 °C under nitrogen protection. $Bi_2WO_6$ is the original raw material synthesized by hydrothermal reaction without any treatment. The degradation of phenol activity using g-$C_3N_4$/$Bi_2WO_6$ and $Bi_2WO_6$-2 have no apparent increase compared with that of $Bi_2WO_6$ nanosheet. The results sufficiently demonstrate that the formation of the core-shell structure facilitates the charge transfer efficiency in the interface of g-$C_3N_4$@$Bi_2WO_6$ and thus significantly improve the catalytic degradation activity.

With calcination temperature increasing, the photocurrent of g-$C_3N_4$@$Bi_2WO_6$ electrodes increase remarkably with the annealing temperature rise from 100 °C to 200 °C, showing an order of samples at 200 > 100 > 300 °C (Fig. 3c). The sample of g-$C_3N_4$@$Bi_2WO_6$ obtained at 200 °C exhibits the highest photocurrent response intensity, which is increased by 3.5 times higher than that of g-$C_3N_4$ and 2.3 times higher compare to $Bi_2WO_6$. The increase of photocurrent indicates that there may exsits chemical bond between g-$C_3N_4$ shell and $Bi_2WO_6$ core, which can promote the separation efficiency of photogenerated carriers resulting a greatly improvement of photocatalytic activity. This law also agrees well with the catalytic activity of phenol degradation.

The optimized g-$C_3N_4$@$Bi_2WO_6$ core-shell photocatalyst is selected to carry out the cycling experiments of photocatalytic degradation of phenol under visible light irradiation. As shown in Fig. 3d the removal degree of phenol by g-$C_3N_4$@$Bi_2WO_6$ core-shell photocatalyst are 30%, 26% and 25% during three-round continuous photo-degradation process, which indicates the g-$C_3N_4$@$Bi_2WO_6$ core-shell photocatalyst has well stability in whole experimental operation process. And the photodegradation activity in subsequent two rounds tests exhibits no obviously decline compared with that of the first experiment, due to the g-$C_3N_4$@$Bi_2WO_6$ core-shell structure could be recycled completely without lost in the process of centrifugal separation. The reproducibility of the new synthesis strategy for g-$C_3N_4$@$Bi_2WO_6$ core-shell structure photocatalyst is investigated, the three samples fabricated in parallel synthesis process are used in the experiment of phenol degradation under visible light irradiation. The removal degree of phenol by the three core-shell structure samples are 26%, 30% and 30% (shown in Fig. S4), indicating the new method of forming g-$C_3N_4$@$Bi_2WO_6$ core-shell structure by the polymerization of CN small molecules into large conjugated structures at low temperature has well repeatability. In order to comprehensive investigate the influence factors on the activity of core-shell photocatalyst, we study the effect of different hydrothermal temperatures on the preparation of CN transparent solution and different CN contents on the photocatalytic activity of g-$C_3N_4$@$Bi_2WO_6$ core-shell photocatalyst. As can be seen from Fig. S6, the CN transparent solution could be prepared under the hydrothermal reaction conditions of 210 °C and 200 °C. The phenol degradation activity gradually decrease with the temperature of the prepared CN decreasing, thus the optimum hydrothermal temperature is 210 °C. As shown in Fig. S7, the phenol degradation activity of g-$C_3N_4$@$Bi_2WO_6$ photocatalyst gradually increases with the decrease of CN content, when the CN content is 13 wt% g-$C_3N_4$@$Bi_2WO_6$ photocatalyst has three molecular layers of g-$C_3N_4$ on the surface of $Bi_2WO_6$ leading to an excellent seperation efficiency of photogenerated carriers and corresponding outstanding catalytic activity.

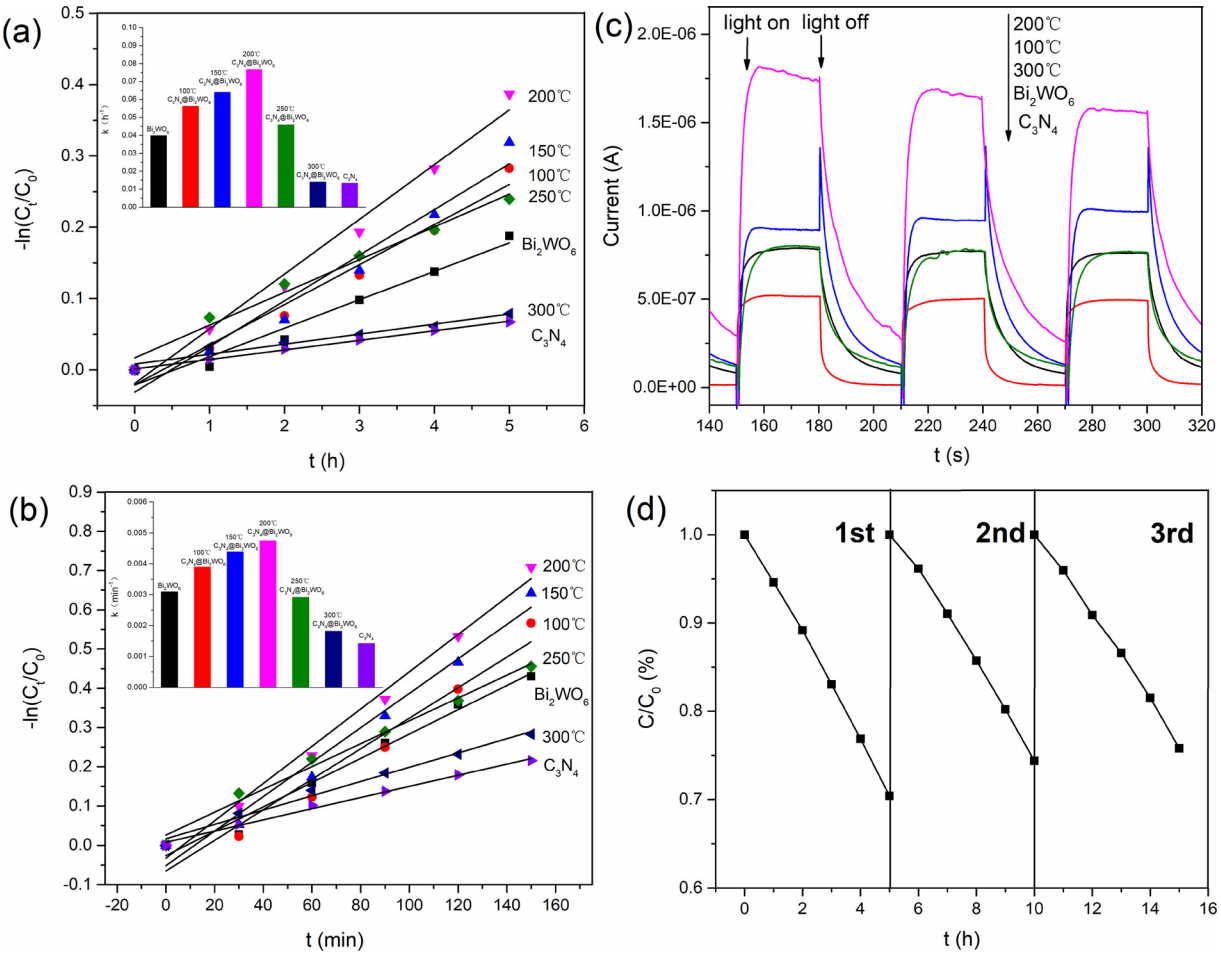


**Fig. 3.** Photocatalytic activity of phenol over g-$C_3N_4$@$Bi_2WO_6$ core-shell photocatalyst (a) visible light ($\lambda_{Vis} \geq 420$ nm), (b) full spectrum, (c) the transient photocurrent density responses of g-$C_3N_4$@$Bi_2WO_6$ core-shell photocatalyst and (d) recycle experiment over g-$C_3N_4$@$Bi_2WO_6$ photocatalyst obtained at 200 °C.

### 3.3. Mechanism of photocatalytic activity enhancement

#### 3.3.1. Photoluminescence spectra and AC impedance spectra

The separation, migration and recombination process of photogenerated carriers in g-$C_3N_4$@$Bi_2WO_6$ core-shell photocatalyst is investigated by the PL technique. As shown in Fig. 4a, the fluorescence emission spectrum of pure g-$C_3N_4$ has a maximum emission peak at 460 nm with a strong broad range (430–550 nm), due to the recombination of photogenerated electrons-holes generated by g-$C_3N_4$ material under photoexcitation. The intensity of fluorescence spectra at 460 nm by g-$C_3N_4$@$Bi_2WO_6$ core-shell photocatalyst remarkably decrease, which mainly results from the lower recombination rate in the interface of the core-shell structure. It can be inferred that photogenerated electrons and holes could transfer from $Bi_2WO_6$ core to g-$C_3N_4$ shell reducing their recombination probability.

In order to further elucidate the mechanism of photocatalytic activity enhancement, the interface charge separation efficiency is investigated by the electrochemical impedance spectroscopy (EIS). It can be seen in Fig. 4b that the arc radiuses of the AC impedance spectra measured under the light irradiation are smaller than that without light irradiation conditions, indicating that all of pure $Bi_2WO_6$, bulk g-$C_3N_4$ and g-$C_3N_4$@$Bi_2WO_6$ core-shell photocatalyst have excellent photoelectric response. Moreover, the resistance of the equivalent circuit elements of the electrochemical system fitting using core-shell photocatalyst is smaller than both pure $Bi_2WO_6$ and bulk g-$C_3N_4$ with light irradiation, indicating that photoelectric response performance of the g-$C_3N_4$@$Bi_2WO_6$ core-shell photocatalyst exhibits better than that of pure $Bi_2WO_6$ and bulk g-$C_3N_4$ with light irradiation. Therefore, the core-shell catalyst could greatly improve the photocatalytic activity by facilitating the separation and migration of charges at the interface.

#### 3.3.2. Photocatalytic mechanism

In order to elucidate the photocatalytic degradation mechanism, it is necessary to detect the main oxidative species in photocatalytic degradation process. So ESR of g-$C_3N_4$@$Bi_2WO_6$ core-shell photocatalyst is shown in Fig. 5. There exists no obvious peak of hydroxyl radicals (·OH) and superoxide radicals ($\cdot O_2^-$) in the absence of light irradiation. Under the visible light, the ESR signal intensities of g-$C_3N_4$@$Bi_2WO_6$ core-shell structure material exhibit a significant enhancement of ·OH and $\cdot O_2^-$ crack peak compared to pure $Bi_2WO_6$ and bulk g-$C_3N_4$, which indicates that the formation of core-shell structure could improve the oxidation capacity. Combined with the above results, it is well recognized that ·OH, $\cdot O_2^-$ and hole ($h^+$) can be produced during the photocatalytic process and play important role in the degradation of phenol. On the basis of the above results, a possible mechanism for the photogenerated charge transfer route of g-$C_3N_4$@$Bi_2WO_6$ core-shell photocatalyst is proposed. As shown in Fig. 5c, photogenerated electrons and holes are generated on CB and VB of g-$C_3N_4$@$Bi_2WO_6$ core-shell photocatalyst under visible irradiation. The CB of $Bi_2WO_6$ core is lower than that of g-$C_3N_4$ shell, so the photogenerated electrons can be injected easily from g-$C_3N_4$ shell into the $Bi_2WO_6$ core. And the VB of $Bi_2WO_6$ core is lower than that of g-$C_3N_4$ shell, the photogenerated holes can be transfered from $Bi_2WO_6$ core into the g-$C_3N_4$ shell [25]. When $O_2$ gas encounters the electrons of $Bi_2WO_6$ to generate $\cdot O_2^-$ and the holes on the VB of g-$C_3N_4$ shows strong oxide capability, which contributes to the enhancement on phenol degradation activity of g-

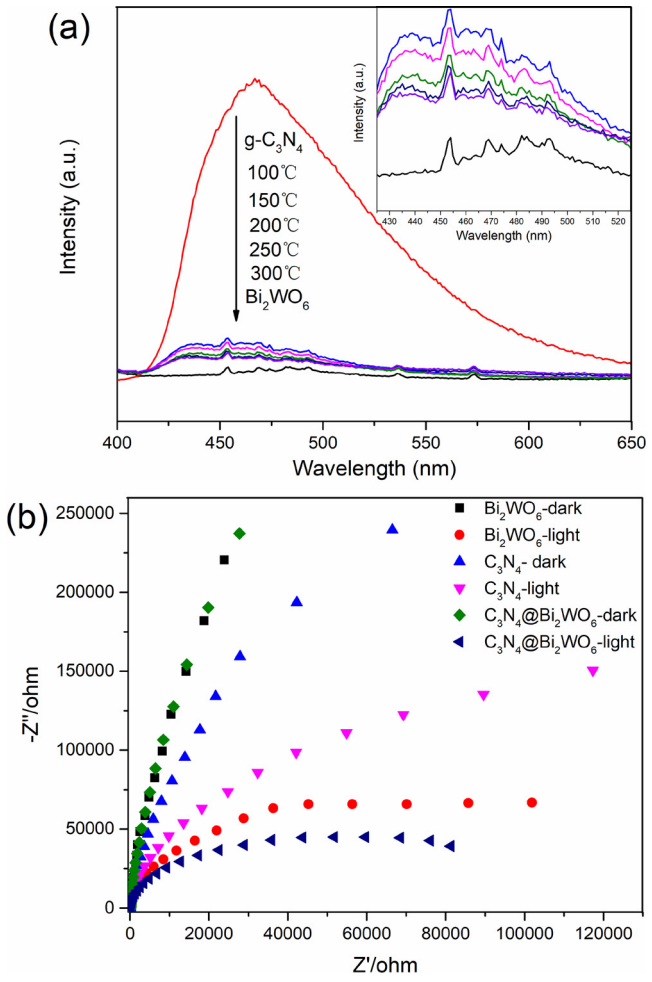


**Fig. 4.** (a) PL spectra of g-$C_3N_4$, $Bi_2WO_6$ and g-$C_3N_4$@$Bi_2WO_6$ core-shell photocatalyst; (b) EIS Nynquist plots of g-$C_3N_4$, $Bi_2WO_6$ and g-$C_3N_4$@$Bi_2WO_6$ core-shell photocatalyst with light on/off cycles under visible light irradiation ($\lambda_{Vis} \geq 420$ nm) [$Na_2SO_4$ = 0.1 M].

$C_3N_4$@$Bi_2WO_6$ core-shell photocatalyst. The g-$C_3N_4$@$Bi_2WO_6$ core-shell structure photocatalyst with 1 nm thickness of shell layers has the highest visible light photocatalytic degradation phenol activity which is almost 5.7 times as high as that of bulk g-$C_3N_4$ and also 1.9 times compare to $Bi_2WO_6$ nanosheet.

## 4. Conclusion

The g-$C_3N_4$@$Bi_2WO_6$ core-shell structure photocatalyst are successfully fabricated by the new method of combining a transparent CN precursor *in situ* coating and low temperature reassembled strategy. This method provides more possibilities for modulation and management on the interface of g-$C_3N_4$@$Bi_2WO_6$ which can accelerate the separation of photogenerated electron-hole pairs. The g-$C_3N_4$@$Bi_2WO_6$ core-shell structure photocatalyst has the highest visible light photocatalytic degradation phenol activity which is almost 5.7 times as high as that of bulk g-$C_3N_4$ and also 1.9 times compare to $Bi_2WO_6$ nanosheet The establishment of g-$C_3N_4$@$Bi_2WO_6$ core-shell photocatalyst system can offer blueprints for the construction of other new interface electric field catalytic system and a new catalytic concept namely the interface electric field catalytic system.

## Acknowledgments

This work was partly supported by National Natural Science

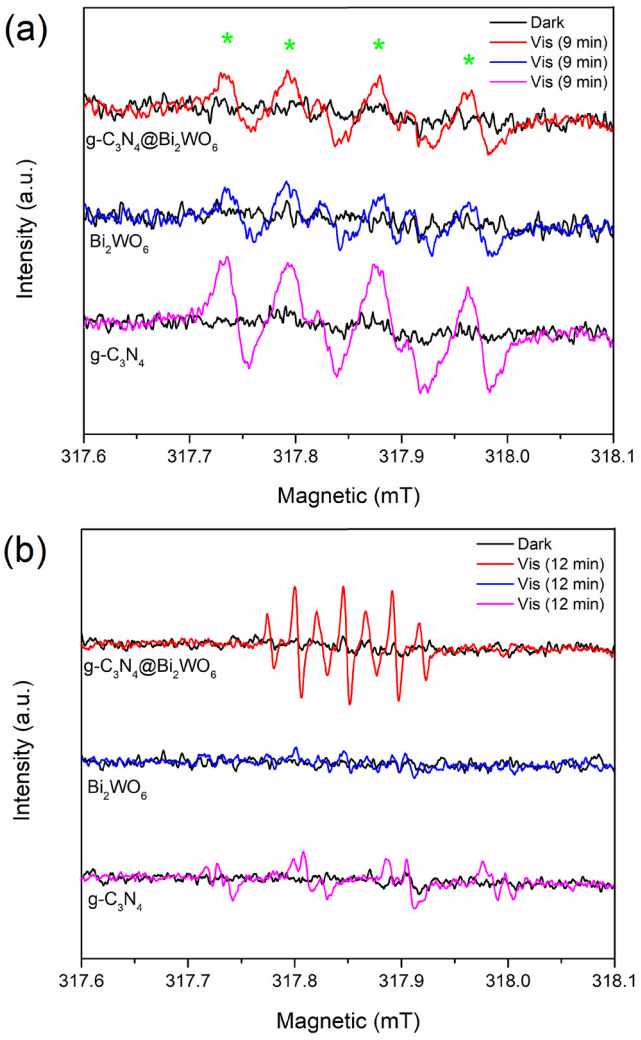


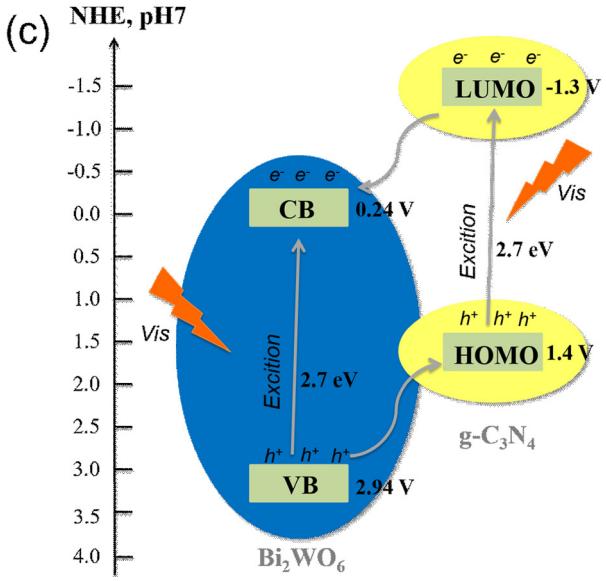


**Fig. 5.** ESR of g-$C_3N_4$, $Bi_2WO_6$ and g-$C_3N_4$@$Bi_2WO_6$ photocatalyst ($\lambda_{Vis} \geq 420$ nm) (a) Superoxide radical test in methanol with DMPO (50 mM) as radical trapper, (b) Hydroxyl radical test in aqueous with DMPO (50 mM) as radical trapper and (c) schematic illustration of electron hole separation over g-$C_3N_4$@$Bi_2WO_6$ photocatalyst ($\lambda_{Vis} \geq 420$ nm).

Foundation of China (21437003, 21673126, 21761142017, 21621003) and Collaborative Innovation Center for Regional Environmental Quality.

## Appendix A. Supplementary data

Supplementary material related to this article can be found, in the online version, at doi:https://doi.org/10.1016/j.apcatb.2018.06.013.

## References

[1] J. Sheng, X. Li, Y. Xu, ACS Catal. 4 (2014) 732–737.
[2] Y. Zhu, Y. Wang, Q. Ling, Y. Zhu, Appl. Catal. B-Environ. 200 (2017) 222–229.
[3] C. Li, G. Chen, J. Sun, H. Dong, Y. Wang, C. Lv, Appl. Catal. B-Environ. 160–161 (2014) 383–389.
[4] J. Tian, Y. Sang, G. Yu, H. Jiang, X. Mu, H. Liu, Adv. Mater. 25 (2013) 5075–5080.
[5] F. Chen, D. Li, B. Luo, M. Chen, W. Shi, J. Alloys Compd. 694 (2017) 193–200.
[6] X.Y. Kong, W.L. Tan, B.-J. Ng, S.-P. Chai, A.R. Mohamed, Nano Res. 10 (2017) 1720–1731.
[7] D. Zhang, J. Li, Q. Wang, Q. Wu, J. Mater. Chem. A 1 (2013) 8622.
[8] M. Zhang, R. Sun, Y. Li, Q. Shi, L. Xie, J. Chen, X. Xu, H. Shi, W. Zhao, J. Phys. Chem. C 120 (2016) 10746–10756.
[9] M. Qamar, R.B. Elsayed, K.R. Alhooshani, M.I. Ahmed, D.W. Bahnemann, ACS Appl. Mater. Interfaces 7 (2015) 1257–1269.
[10] H. Huang, Y. He, Z. Lin, L. Kang, Y. Zhang, J. Phys. Chem. C 117 (2013) 22986–22994.
[11] Y. Chen, J. Fang, S. Lu, W. Xu, Z. Liu, X. Xu, Z. Fang, J. Chem. Technol. Biotechnol. 90 (2015) 947–954.
[12] D. He, L. Wang, D. Xu, J. Zhai, D. Wang, T. Xie, ACS Appl. Mater. Interfaces 3 (2011) 3167–3171.
[13] M. Li, L. Zhang, X. Fan, Y. Zhou, M. Wu, J. Shi, J. Mater. Chem. A 3 (2015) 5189–5196.
[14] Y. Zhou, Z. Tian, Z. Zhao, Q. Liu, J. Kou, X. Chen, J. Gao, S. Yan, Z. Zou, ACS Appl. Mater. Interfaces 3 (2011) 3594–3601.
[15] S. Zhu, T. Xu, H. Fu, J. Zhao, Y. Zhu, Environ. Sci. Technol. 41 (2007) 6234–6239.
[16] R.M. Mohamed, E.S. Aazam, Mater. Res. Bull. 48 (2013) 3572–3578.
[17] H. Yu, R. Liu, X. Wang, P. Wang, J. Yu, Appl. Catal. B-Environ. 111–112 (2012) 326–333.
[18] L. Ge, J. Liu, Appl. Catal. B-Environ. 105 (2011) 289–297.
[19] D. Wang, L. Guo, Y. Zhen, L. Yue, G. Xue, F. Fu, J. Mater. Chem. A 2 (2014) 11716–11727.
[20] G. Fu, G. Xu, S. Chen, L. Lei, M. Zhang, Catal. Commun. 40 (2013) 120–124.
[21] X. Wang, K. Maeda, A. Thomas, K. Takanabe, G. Xin, J.M. Carlsson, K. Domen, M. Antonietti, Nat. Mater. 8 (2009) 76–80.
[22] L. Lin, W. Ren, C. Wang, A.M. Asiri, J. Zhang, X. Wang, Appl. Catal. B-Environ. 231 (2018) 234–241.
[23] F. Guo, Y. Hou, A.M. Asiri, X. Wang, Chem. Commun. 53 (2017) 13221–13224.
[24] L. Lin, C. Wang, W. Ren, H. Qu, Y. Zhang, X. Wang, Chem. Sci. 8 (2017) 5506–5511.
[25] Y. Cui, Z. Ding, X. Fu, X. Wang, Angew. Chem. Int. Ed. 51 (2012) 11814–11818.
[26] J. Sun, J. Zhang, M. Zhang, M. Antonietti, X. Fu, X. Wang, Nat. Commun. 3 (1139) (2012) 1–7.
[27] C. Yang, B. Wang, L. Zhang, L. Yin, X. Wang, Angew. Chem. 129 (2017) 6727–6731.
[28] Y. Zheng, Z. Yu, H. Qu, A.M. Asiri, Y. Chen, X. Wang, Adv. Funct. Mater. 28 (1705407) (2018) 1–9.
[29] X. Bai, R. Zong, C. Li, D. Liu, Y. Liu, Y. Zhu, Appl. Catal. B-Environ. 147 (2014) 82–91.
[30] D. Chen, K. Wang, D. Xiang, R. Zong, W. Yao, Y. Zhu, Appl. Catal. B-Environ. 147 (2014) 554–561.
[31] C. Pan, J. Xu, Y. Wang, D. Li, Y. Zhu, Adv. Funct. Mater. 22 (2012) 1518–1524.
[32] Y. Wang, X. Bai, C. Pan, J. He, Y. Zhu, J. Mater. Chem. 22 (2012) 11568.
[33] Y. Wang, W. Yang, X. Chen, J. Wang, Y. Zhu, Appl. Catal. B-Environ. 220 (2018) 337–347.
[34] G. Zhang, C. Huang, X. Wang, Small 11 (2015) 1215–1221.
[35] D. Zheng, C. Pang, Y. Liu, X. Wang, Chem. Commun. 51 (2015) 9706–9709.
[36] D. Zheng, G. Zhang, Y. Hou, X. Wang, Appl. Catal. A-Gen. 521 (2016) 2–8.